Molecular insights into the μ-opioid receptor selective signaling

Xiaojing Cong,[1,#] Damien Maurel,[1,#] Héléne Déméné,[2] Ieva Vasiliauskaité-Brooks,[1] Joanna Hagelberger,[1] Fanny Peysson,[1] Julie Saint-Paul,[1] Jérôme Golebiowski,[3,4] Sébastien Granier,[1,*] and Rémy Sounier[1,5,*]

[1]Institut de Génomique Fonctionnelle, CNRS UMR-5203 INSERM U1191, University of Montpellier, F-34000 Montpellier, France.
[2]Centre de Biochimie Structurale, CNRS UMR 5048-INSERM 1054- University of Montpellier, 29 rue de Navacelles, 34090 Montpellier Cedex, France.
[3]Université Côte d'Azur, CNRS, Institute of Chemistry of Nice UMR7272, F-06108 Nice, France.
[4]Department of Brain and Cognitive Sciences, Daegu Gyeongbuk Institute of Science and Technology, Daegu 711-873, South Korea.
[5]Lead contact.
[#]These authors contributed equally.
*Correspondence: sebastien.granier@igf.cnrs.fr (S.G.) or remy.sounier@igf.cnrs.fr (R.S.)

SUMMARY

GPCR functional selectivity whereby a ligand discriminates specific signaling pathways has opened new opportunities for the design of safer drugs. Ligands orchestrate GPCR signaling cascades by modulating the receptor conformational landscape. Our study provides insights into the dynamic mechanism enabling opioid ligands to selectively activate the G protein over the β-arrestin pathways through the μ-opioid receptor (μOR). We combined functional assays in living cells, solution NMR spectroscopy and enhanced-sampling molecular dynamic simulations to identify the specific μOR conformations induced by G protein-selective agonists. In particular, we describe the dynamic and allosteric communications between the ligand-binding pocket and the receptor intracellular domains, through conserved motifs in class A GPCRs. Most strikingly, the selective agonists triggered μOR conformational changes in the intracellular loop 1 and helix 8 domains, which may impair β-arrestin binding or signaling. The findings may apply to other GPCR families and provide key molecular information that could facilitate the design of selective ligands.

INTRODUCTION

Cell signaling relies on second messenger systems that are modulated by G protein-coupled receptors (GPCRs) in a ligand-specific manner. GPCRs are known for the complexity of their signaling pathways and conformational landscape. Ligands may selectively active or inhibit distinct signaling pathways, by changing the conformations of the GPCR (Weis and Kobilka, 2018). This is known as functional selectivity (or ligand bias), which provides fine regulations of GPCR functions and new drug design opportunities. Functional selectivity of the μ-opioid receptor (μOR) is among the most studied, in a global effort to develop safer analgesics. Opioid analgesics are efficacious and inexpensive, however, their severe side effects caused the ongoing opioid epidemic starting from the 1990s. A number of studies from 2005 to 2010 associated major opioid side effects with the β-arrestin signaling pathways (reviewed in (Raehal et al., 2011)), which has driven over a decade of research for G protein-selective μOR agonists. This led to the discovery of TRV130 (oliceridine) (DeWire et al., 2013) and PZM21 (Manglik et al., 2016), two G protein-selective agonists showing less side effects than morphine in early studies. Oliceridine was approved by the FDA in 2020 for pain management, however, it still has typical opioid side effects such as nausea, vomiting, dizziness, headache, and constipation. There are high expectations on PZM21, which outperformed TRV130 and morphine in mice (Manglik et al., 2016). Nevertheless, recent findings argue that G-protein selectivity may improve

analgesia and tolerance but not necessarily the side effects (Kliewer et al., 2019). Opioid-induced respiratory depression and constipation could be independent of β-arrestin signaling (Kliewer et al., 2020). It was suggested that the favorable therapeutic profiles of TRV130 and PZM21 are due to low efficacy rather than functional selectivity (Gillis et al., 2020; Yudin and Rohacs, 2019). Yet, G protein selectivity correlates with broader therapeutic windows, enabling better separations of the beneficial and adverse opioid effects (Schmid et al., 2017). A potential explanation for these discrepancies is the weak selectivity of these ligands compared to the complexity of the GPCR signaling network (Conibear and Kelly, 2019). The diversity of the systems used may also be a source of inconsistency. There is a pressing need of strongly biased and highly specific ligands, to probe the μOR signaling network for more insights. Finding such probes demands understanding the molecular mechanism of functional selectivity, which is intrinsic to the GPCR. However, GPCRs are not static on-off switches but complex molecular machines which operate through strictly regulated motions (Weis and Kobilka, 2018). Functional selectivity relies on the dynamic equilibrium of GPCR conformations, which is so far poorly understood.

X-ray crystallography and cryoEM have successfully captured inactive and active μOR states(Huang et al., 2015; Koehl et al., 2018; Manglik et al., 2012). Yet, they represent essentially a few snapshots of the vast landscape of GPCR conformations. The active states of ternary complexes exhibit a large outward displacement of the transmembrane helix 6 (TM6), which requires stabilization by G proteins or G protein-mimetics (reviewed in (Weis and Kobilka, 2018)). Conformational changes induced by ligand-binding, however, are very subtle and dynamic, as revealed by recent NMR studies on the β2-adrenergic receptor (β2AR) (Manglik et al., 2015; Nygaard et al., 2013) and on μOR (Okude et al., 2015; Sounier et al., 2015). Agonist binding initiate slight conformational changes in the ligand-binding domain (LBD), sufficient to trigger long-range conformational changes via the connector region (CR) until the intracellular coupling domains (ICD), in an allosteric and dynamic manner. Signaling partners (e.g. G proteins or β-arrestins) couple to the activated ICD and induce further large-scale opening of ICD to a fully-active state. This activation process is common in various GPCRs such as the leukotriene B4 receptor BLT2 (Casiraghi et al., 2016), the β1-adrenergic receptor (β1AR) (Isogai et al., 2016), the adenosine A_{2A} receptor (Clark et al., 2017; Eddy et al., 2018; Ye et al., 2016) and the muscarinic M2 receptor (M2R) (Xu et al., 2019). However, detailed activation dynamics, especially the mechanism of functional selectivity, are difficult to capture by X-ray crystallography or cryoEM. NMR spectroscopy has proven to be particularly suitable for monitoring subtle dynamic conformational transitions during GPCR activation (Kofuku et al., 2014; Liang et al., 2018; Shimada et al., 2019). MD on the other side has provided insightful details of the potential activation processes (Latorraca et al., 2017). Here, we combined a thorough functional investigation of agonists, NMR spectroscopy and molecular dynamics (MD) simulations to obtain atomistic-level descriptions on μOR agonism. To this end, we have established a dual isotope labeling NMR scheme for μOR based on our previous study (Sounier et al., 2015). For the MD, we used the REST2 enhanced sampling scheme (REST2-MD), which has proven efficient in monitoring GPCR activation (Cong et al., 2019; Cong et al., 2018; Cong and Golebiowski, 2018; Sena et al., 2017).

We studied five chemically distinct μOR agonists (**Figure 1A**): DAMGO, a well-characterized μOR-specific peptide (Emmerson et al., 1994; Handa et al., 1981); buprenorphine, a semi-synthetic thebaine analogue and partial agonist (Cowan et al., 1977a; Cowan et al., 1977b); BU72, a potent buprenorphine derivative (Neilan et al., 2004); as well as the aforementioned selective agonists, TRV130 and PZM21. By comparing the effects of these agonists on the μOR conformational dynamics, we provide here unprecedented insights into the molecular mechanism of μOR functional selectivity.

RESULTS

Opioids signaling in living cells

We first characterized the functional profiles of the five opioids in cell-based assays for their abilities to bind the target, to activate G proteins (Gi/o) and GPCR kinase 2 (GRK2), to recruit β-arrestins, and to trigger μOR internalization. Using advanced fluorescence methods, we probed i) competitive ligand

binding to the target cells and μOR against naloxone, ii) dissociation of the G protein heterotrimer, iii) ligand-induced μOR interactions with GRK2 or iv) with β-arrestins, and v) diminution of cell-surface μORs (internalization) (**Figures 1B—1F and S1; Table 1**).

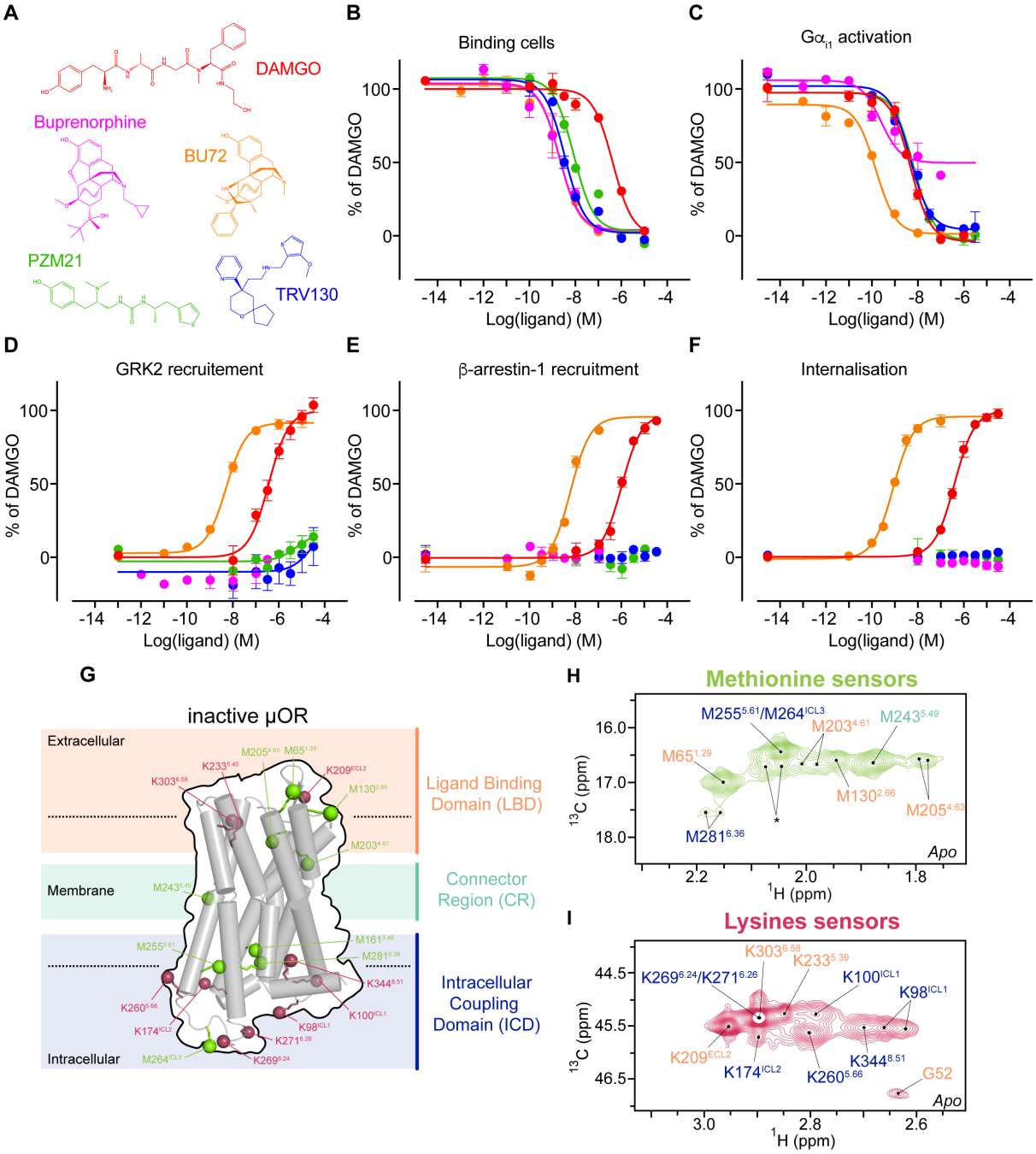

Figure 1. Functional characterizations of the μOR agonists and development of multi-domain NMR sensors.

(**A**) Chemical structures of the five agonists. (**B—F**) Dose-dependent response curves of the agonists in (B) competitive binding against fluorescent naltrexone in living cells, (C) activating $G\alpha_{i1}$, (D) inducing GRK2 recruitment, (E) inducing β-arrestin1 recruitment, and (F) inducing μOR internalization. Color code in (B—F) is the same than (A). Data shown are the means ± SEM of a representative experiment performed in triplicates normalized to the maximal response induced by DAMGO and fitted using an operational model of agonism. (**G**) Location of the NMR sensors in a cartoon representation of μOR in inactive form. NMR sensors, ε-CH_3 of methionine (green) and ε-NH_2 of lysine (raspberry), are shown in balls, in the ligand binding domain (LBD, pale orange), the connector region (CR, pale green) and the intracellular coupling domain (ICD, blue). (**H** and **I**) Extracted 2D HMQC spectra of the methionine and lysine sensors, as well as the backbone amine of the N-terminal residue G52, in *apo* μOR. Asterisk indicates the peak positions of residual resonances of the N-terminal methionine in a small amount of untruncated μOR.

All the five opioids behaved as agonists in the Gi_{1-2-3} and Go_{a-b} activation assays (**Figures 1C and S1A—S1D**). Compared to DAMGO (our reference ligand), buprenorphine was the only partial agonist, showing 63 ± 9% to 83 ± 10 % of Efficacy even at saturating concentration (**Figures 1B—1C and S1A—S1D; Table S1)**. This agrees with the literature data from [^{35}S]-GTPγS binding experiments (Traynor and Nahorski, 1995). Concerning GRK2, β-arrestins, and μOR internalization, DAMGO and BU72 showed comparable efficacies with the latter being more potent (**Figures 1D—1F and S1E; Table S1).** TRV130, PZM21 and buprenorphine had negligible or no effects on these signaling pathways. Therefore, DAMGO and BU72 behaved as unselective full agonists, TRV130 and PZM21 were G protein-selective full agonists, while buprenorphine was a G protein-selective partial agonist. Note that we avoided quantification of the ligand bias factors, e.g. measuring the degrees of selectivity in different cell systems. Instead, the agonists were categorized to facilitate the NMR and REST2-MD analyses below.

Development of multidomain NMR sensors for allosteric GPCR motions.

We used a previously established mouse μOR construct for NMR spectroscopy, which contained an M72$^{1.36}$T mutation (superscript refers to the Ballesteros-Weinstein numbering) that increased the expression level and reduced the NMR peak overlaps (Sounier et al., 2015). The N-terminus was truncated before residue G52. This μOR construct maintained intact μOR functions and was stable for the duration of the NMR experiments (Sounier et al., 2015) (**Figures S1F and S2A**). Our previous approach used lysine sensors to probe μOR motions in the solvent-accessible domains (Sounier et al., 2015). Here we developed a novel dual-isotope methyl labeling scheme to monitor the solvent-accessible domains and the 7-transmembrane helices (7TM) simultaneously**.** For this purpose, we introduced NMR-active ^{13}C probes into methionines (biosynthetically) and lysines (through reductive methylation) of the μOR construct. The heteronuclear multiple-quantum coherence (HMQC) pulse sequences were used to obtain 2D ^{1}H-^{13}C chemical shift correlation maps (see Methods). We unambiguously assigned the $^{13}CH_3$-ε-methionine and the dimethylamine peaks to twenty sensors in the unliganded (*apo*) μOR: the G52 backbone amine at the N-terminus, three lysines and four methionines in the LBD, one methionines in the CR, as well as seven lysines and four methionines in the ICD (**Figures 1G—1I and S2B**).

To monitor agonist-induced μOR activation, we collected the HMQC spectra of μOR bound to each agonist, with and without the G protein-mimetic nanobody, Nb33 (**Figures 1G—1I and S2C—S2E**). Nb33 was necessary to reach the fully active state of μOR (Sounier et al., 2015), whereas without Nb33 we obtained the intrinsic effects of the agonist binding, more likely to reflect the mechanism of functional selectivity. The agonists and Nb33 have high affinities for μOR (< 0.1 μM). At saturating concentrations (30 μM, 60 μM and 150 μM for μOR, Nb33 and the agonists, respectively), according to the law of mass action, 99% of the μORs should be in complexes at 10 μM concentration of the agonists and Nb33 (~100 times the K_d concentration). Hence, we assumed that all the μORs were in ternary receptor-agonist-Nb33 complexes during the NMR measurements.

Allosteric cooperation between the agonists and the G protein binding site

Upon binding of the agonists alone, the LBD sensors M65$^{1.29}$ and M205$^{4.63}$ exhibited multiple peaks with different intensities, which varied among the five agonists (**Figure S3)**. This indicates intermediate-to-slow exchanges among multiple conformations of the receptor and/or the agonists on the NMR timescales. Nb33 binding at the ICD caused more drastic changes of the NMR signals in the LBD (including the N-terminus and the extracellular loop 2 (ECL2)), in a ligand-dependent manner (**Figure S3)**. This indicates allosteric communications between the agonists and the Nb33, and between the LBD and the ICD, upon receptor activation. Allosteric cooperation between the LBD and the ICD has been reported for other class A GPCRs (Eddy et al., 2018; Liu et al., 2017; Liu et al., 2019a).

At the G protein binding site (at TM5/ICL3/TM6 in the ICD), the five agonists induced only small conformational changes (**Figure S4)**. Nevertheless, the small changes were sufficient for the binding of Nb33, which in turn induced large conformational changes in TM5/TM6 as seen in the crystal

structures of active μOR (Huang et al., 2015) (**Figure S4)**. The magnitudes of the changes in the ternary μOR-agonist-Nb33 complexes correlated with the G-protein efficacies of the agonists (**Figure S4D and S4H**). This suggests that the capacity of an agonist to cooperate with the G proteins allosterically determines its efficacy to active the canonical G protein signaling pathway.

Selective, unselective or partial agonists exhibit different binding poses

To investigate the molecular mechanism of the discrete agonist activities, we performed REST2-MD simulations to examine how each agonist modulates the μOR conformational ensemble. All the simulations were initiated by docking the agonist to the crystal structure coordinates of μOR in an inactive form (PDB: 4DKL) (Manglik et al., 2012) without Nb33. The REST2-MD reproduced the binding poses of DAMGO and BU72 in the cryoEM/crystal structures of μOR in active forms (PDBs 6DDE(Koehl et al., 2018) and 5C1M (Huang et al., 2015), respectively, **Figure S5**). This confirmed sufficient conformational sampling by the REST2-MD in our protocol. The selective agonists, TRV130, PZM21 and buprenorphine, turned out to bind deeper into the CR than DAMGO and BU72. They inserted between W293$^{6.48}$ and TM2, whereas DAMGO and BU72 bound on top of W293$^{6.48}$ (**Figure 2A)**. The REST2-MD also captured alternative, short-lived binding poses of TRV130 and PZM21, in which the ligands bound on top of W293$^{6.48}$ (**Figures S5A—S5B)**. These are likely transient poses in the binding process. Indeed, the HMQC spectra in the LBD indicated exchanges between different receptor/ligand conformations for all the five agonists (**Figure S3**) Whether such transient binding poses contribute to the receptor activation in the ICD is difficult to determine, since the LBD and the ICD are loosely coupled. Therefore, we focus on the ensemble changes in the receptor conformational equilibrium, without interpreting the roles of the transient binding poses.

In the case of buprenorphine, the partial agonist, W293$^{6.48}$ switched between two rotamers, whereas the full agonists maintained mostly one of the W293$^{6.48}$ rotamers like in *apo* μOR (**Figure 2B**). W293$^{6.48}$ is part of the conserved CW$^{6.48}$xP motif in class A GPCRs, known as the “toggle switch” of receptor activation. It is located at the bottom of the orthosteric pocket, on top of the conserved “PIF” motif (P244$^{5.50}$, I155$^{3.40}$, and F289$^{6.44}$) in the CR. Together, they form the so-called “connector region” which mediates the allosteric communications between the LBD and the ICD (Latorraca et al., 2017). W293$^{6.48}$ plays important roles in μOR activation or inhibition (Huang et al., 2015; Yuan et al., 2015). Therefore, the different agonist binding poses with respect to W293$^{6.48}$ may be the initial trigger of the different signaling outcomes.

The above REST2-MD observations were confirmed by the NMR sensor M243$^{5.49}$ in the CR**.** We spotted a distinct pattern in the buprenorphine-μOR complex than in the other systems: the peak of M243$^{5.49}$ shifted upfield in both the ^{1}H and ^{13}C dimensions, as expected from the rotation of W293$^{6.48}$ toward M243$^{5.49}$ upon buprenorphine binding (**Figure 2C)**. Given the well-documented “toggle switch” role of W293$^{6.48}$ in μOR activation (Huang et al., 2015; Yuan et al., 2015), we conclude that the low efficacy of buprenorphine is associated with its low capability to stabilize the required W293$^{6.48}$ rotameric state for activation.

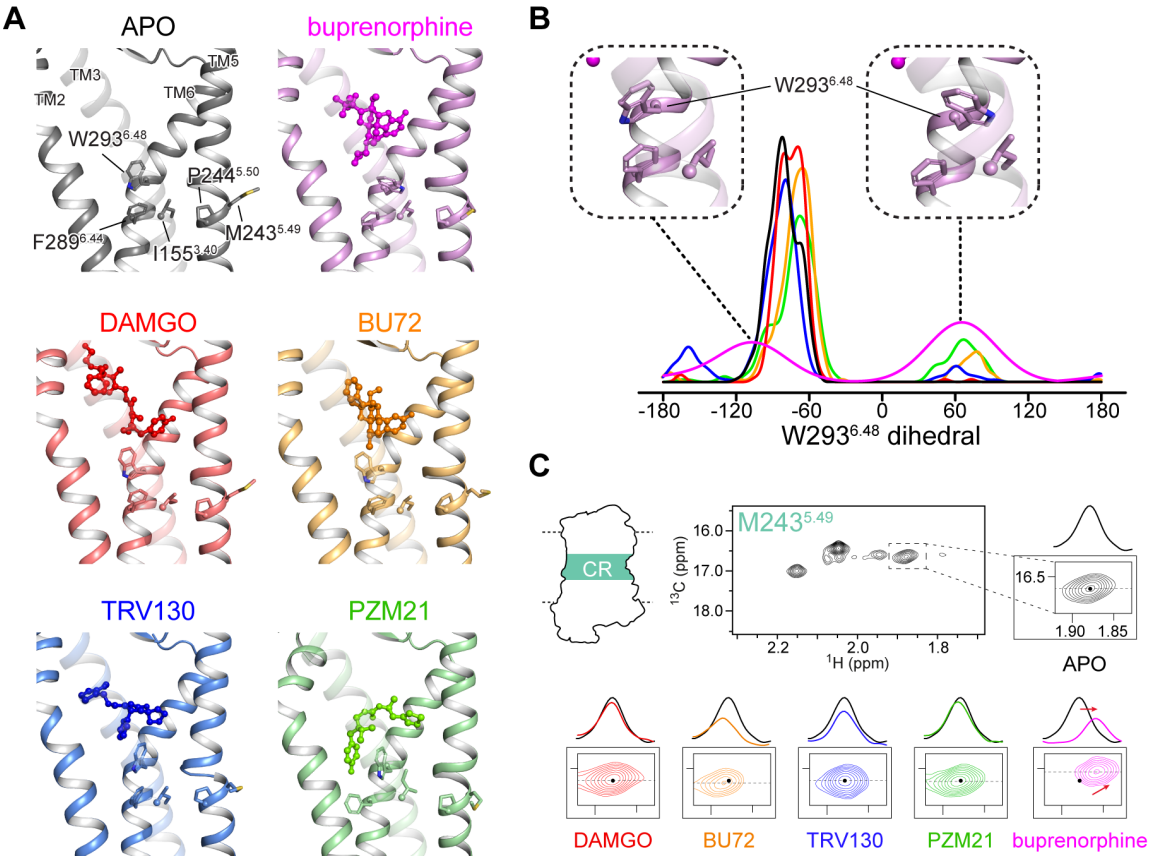

Figure 2. Distinct binding patterns of selective, unselective and partial agonists in comparison with NMR.

(**A**) Unselective agonists (DAMGO and BU72) bind on top of W293$^{6.48}$, whereas selective ones (TRV130, PZM21 and buprenorphine) insert between W293$^{6.48}$ and TM2. The conserved "PIF" motif (P244$^{5.50}$, I155$^{3.40}$ and F289$^{6.44}$) and the NMR sensor M243$^{5.49}$ in the CR are shown in sticks. (**B**) Ligand-dependent rotamers of W293$^{6.48}$, as measured by the distribution of the dihedral angle χ_2 during the REST2-MD simulations. (**C**) Extracted HMQC spectra of M243$^{5.49}$ resonances in *apo* μOR (black) and at saturating concentration of DAMGO (red), BU72 (orange), TRV130 (blue), PZM21 (green) and buprenorphine (magenta). Dashed black lines indicate the position of the cross-sections shown above the spectra.

Conformational changes in the intracellular β-arrestin binding site

The selective agonists TRV130 and PZM21 produced distinct μOR conformations in the lower half of TM7, the intracellular loop 1 (ICL1) and the helix 8 (H8) during the REST2-MD. The simulations revealed an allosteric communication from W293$^{6.48}$ to ICL1 and H8, through the conserved motifs G$^{1.49}$N$^{1.50}$ and N$^{7.49}$P$^{7.50}$xxY$^{7.53}$. Namely, the selective agonists inserted between W293$^{6.48}$ and A117$^{2.53}$ in the CR and split TM6 and TM2, which let TM7 to approach TM3 (**Figures 3A—3C**). The N$^{7.49}$P$^{7.50}$xxY$^{7.53}$ motif in TM7 thus moved toward TM3, away from the G$^{1.49}$N$^{1.50}$ motif in TM1 (**Figures 3C—3E**). This led to remarkable inward movements of TM7 and H8 toward TM3 in the ICD, closing the cleft between H8 and ICL1 (**Figures 4A—4C**). In the case of the unselective agonists (DAMGO and BU72), W293$^{6.48}$ interacted with A117$^{2.53}$ while N$^{7.49}$P$^{7.50}$xxY$^{7.53}$ remained in close contact with G$^{1.49}$N$^{1.50}$. Residues N332$^{7.49}$ and Y336$^{7.53}$ formed a hydrophilic cluster with N86$^{1.50}$ and D114$^{2.50}$. D$^{2.50}$ is the sodium binding site conserved in 90% of non-olfactory class A GPCRs (Katritch et al., 2014) and an important microswitch of receptor activation (Vanni et al., 2010). This configuration resembled those in the initial crystal structure (4DKL) and *apo* μOR (**Figure 3**), so did ICL1 and H8 (**Figures 4A—4C**). The partial selective agonist buprenorphine showed an in-between behavior. In the CR and the N$^{7.49}$P$^{7.50}$xxY$^{7.53}$-G$^{1.49}$N$^{1.50}$ motifs, buprenorphine showed similar but weaker impacts than TRV130 and PZM21 (**Figures 3B and 3E**). The impacts barely reached the ICL1/H8 domains in the simulation timescale (**Figures 4A—4C**).

The NMR spectra in the ICL1/H8 domain confirmed the above findings. DAMGO, BU72 and buprenorphine binding results in the small loss of signal intensity of these sensors in H8/ICL1 (**Figure**

4D). Upon binding the selective agonists TRV130 and PZM21, the lysine sensors K98^{ICL1} and K344$^{8.50}$ showed multiple peaks with change in signal intensity, indicating a much more complex conformational equilibrium (**Figure 4D**). This suggests that the local conformations became more dynamic. Binding of Nb33 led to signal intensity decrease for all the ligands (**Figure S4O—S4P**).

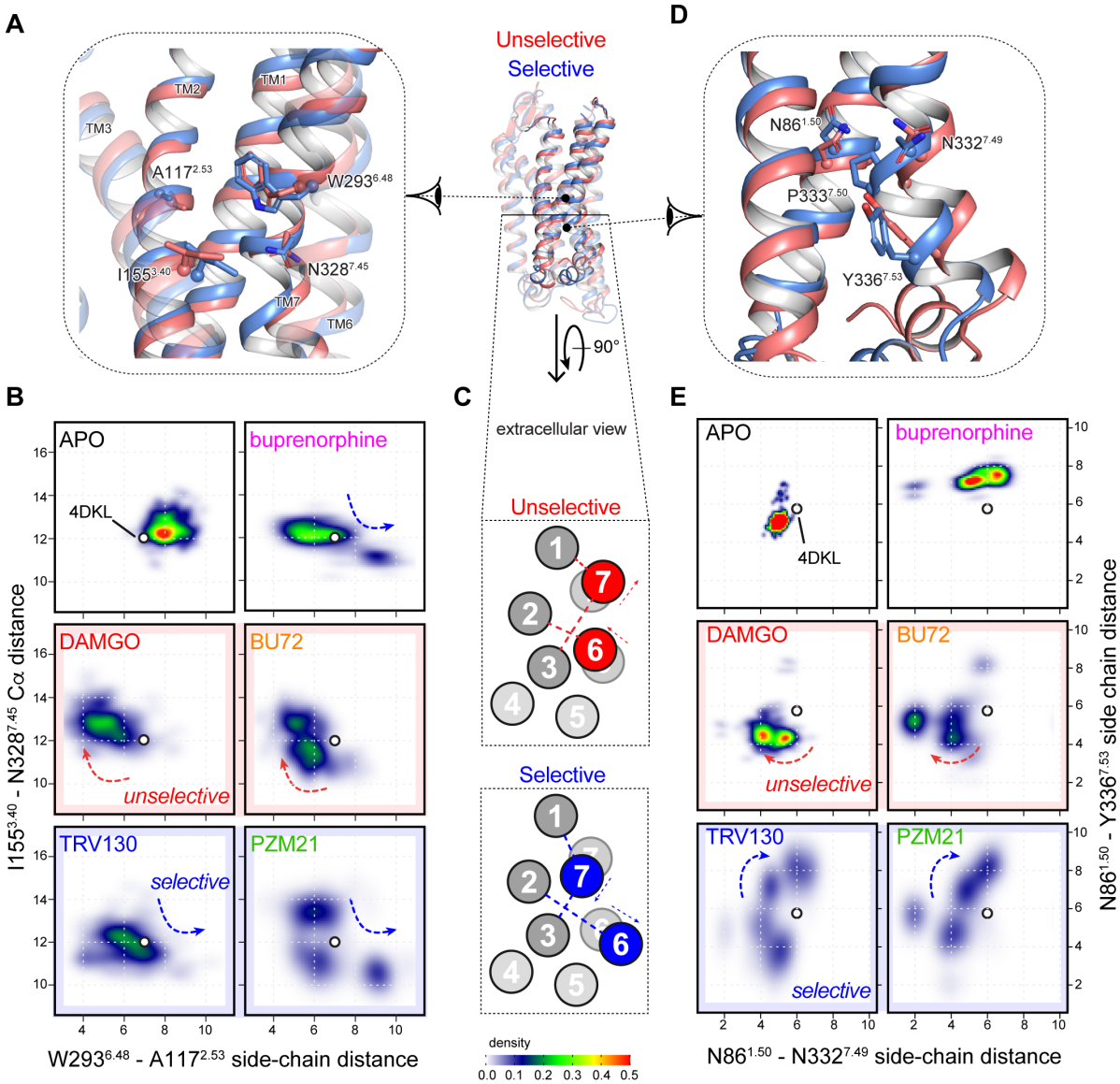

Figure 3. Selective agonists induced conformational changes in the CR and the lower half of TM7.

(**A**) In the CR, selective agonist binding (blue) splits the side chains of W293$^{6.48}$ and A117$^{2.53}$, which allows TM7 to approach TM3. The movements are measured by (**B**) the minimum side-chain distances between W293$^{6.48}$ and A117$^{2.53}$, against the Cα distances between I155$^{3.40}$ and N328$^{7.45}$. (**C**) Schematic presentation of the inter-helical movements. Arrows indicate the direction of the movements and dashed lines indicates the distances measured for (B and E). (**D**) In the lower half of TM7, the N$^{7.49}$P$^{7.50}$xxY$^{7.53}$ motif moves away from the G$^{1.49}$N$^{1.50}$ motif in TM1 only for selective agonists. This is measured by (**E**) the side-chain distances between N86$^{1.50}$, N332$^{7.49}$ and Y336$^{7.53}$.

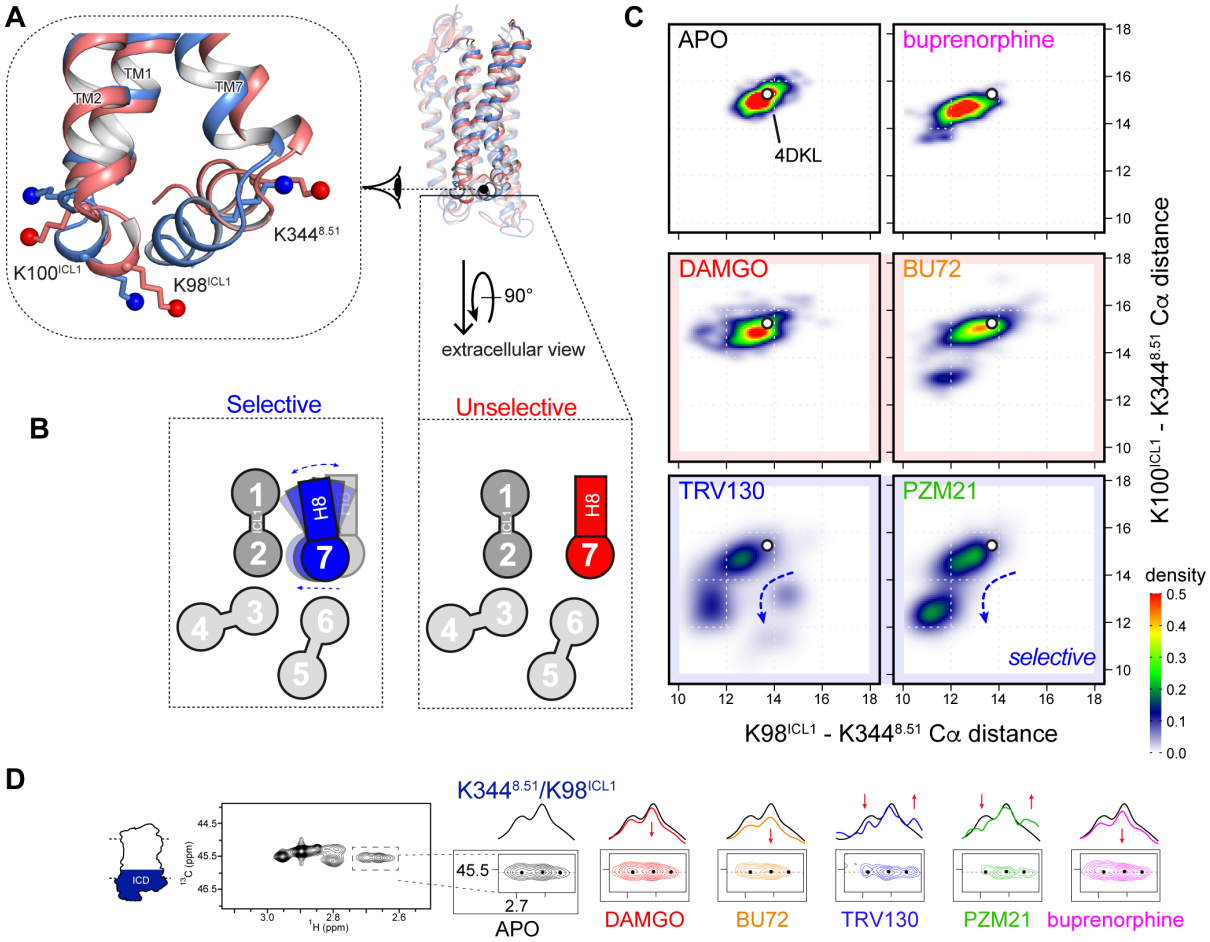

Figure 4. Selective agonists induced new clusters of μOR conformations in ICL1 and H8.

(**A**) Selective agonist binding (blue) triggered inward movements of TM7-H8 toward TM3 and ICL1, respectively, closing the ICL1-H8 cleft. (**B**) Schematic presentation of the movements in (A) from the extracellular view, as measured by (**C**) the Cα distances between the NMR sensors $K98^{ICL1}$, $K100^{ICL1}$ and $K344^{8.51}$. Density maps of the measured distances illustrate a new cluster of conformations associated with the selective agonists TRV130 and PZM21. (**D**) Extracted HMQC spectra of $K344^{8.51}/K98^{ICL1}$ resonances of μOR in *apo* form (black) and at saturating concentrations of DAMGO (red), BU72 (orange), TRV130 (blue), PZM21 (green) and buprenorphine (magenta). Dashed black lines indicate the position of the cross-sections shown above the spectra. Black dots indicate the peak centers in *apo* μOR. Red arrows indicate the changes upon agonist binding.

Overall, the results suggest that the selective agonists act on the toggle switch $W293^{6.48}$ to trigger conformational changes in TM7, ICL1 and H8 in the ICD. This occurs in an allosteric manner, via the conserved motifs $N^{7.49}P^{7.50}xxY^{7.53}$ and $G^{1.49}N^{1.50}$. The conformational changes persist even when the receptor is coupled to Nb33. Although the binding sites of G proteins and arrestins largely overlap, only arrestins interact with ICL1/H8 in the structures of arrestin in complex with rhodopsin, neurotensin receptor 1, β1AR and M2R (Huang et al., 2020; Lee et al., 2020; Staus et al., 2020; Yin et al., 2019). Therefore, the distinct TM7-ICL1-H8 conformations generated by the selective agonists likely inhibit the binding of β-arrestins but not the G proteins (**Figure 5**).

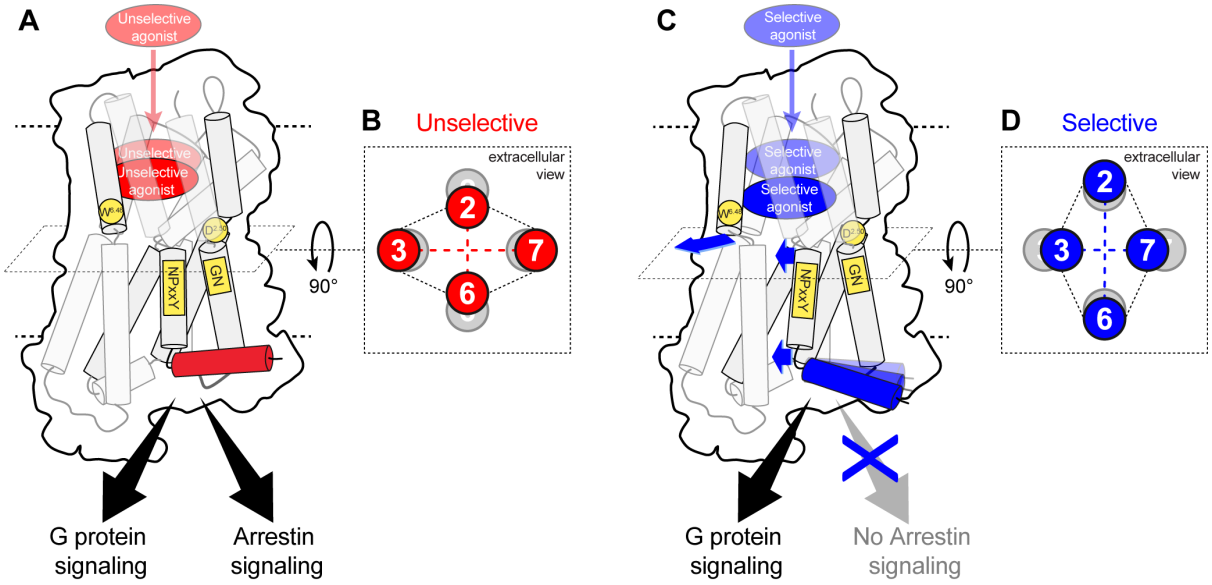

Figure 5. Scheme of the proposed allosteric mechanism of μOR functional selectivity.

(**A**) Binding of the unselective agonists cause W293$^{6.48}$ in TM6 to approach TM2 in (**B**) the connector region. (**C**) Selective agonists bind deeper in the pocket and separate TM6 from TM2 in (**D**) the connector region, letting TM7 to approach TM3. This disrupts the interactions between the NPxxY motif, D114$^{2.50}$ and the GN motif (C). The lower half of TM7 moves toward TM3, closing the cleft between H8 and ICL1, which may inhibit arrestin signaling (C). Blue arrows indicate the movements associated with allosteric functional selectivity. Conserved residues/motifs involved are highlighted in yellow. The transmembrane helices are represented by two adjoining cylinders colored in grey. The top cylinder of TM1 and TM7 are transparent for clarity.

DISCUSSION

The pharmacological outcome of a ligand varies with the test systems and conditions, which have led to contradictory findings and the ongoing debate on whether μOR functional selectivity can separate analgesia from opioid side effects. Even the characterization of functional selectivity itself is debated, due to the lack of deep comprehensions and field standards. In this study, we provide the basic molecular mechanism of selective and partial agonism in μOR, which is intrinsic to the receptor-ligand interactions and should be consistent under different test conditions. The approach and findings can serve as high-resolution monitors for the design and evaluation of μOR ligands with specific functions, e.g. partial or selective agonism/antagonism/inverse agonism for a specific signaling pathway. Such ligands may serve to pinpoint specific aspects of the μOR signaling network, helping resolve the ongoing debates from bottom up. GPCR ligand design is challenging despite the growing number of high-resolution structures. While structure-based design and screening have lifted the hit rate, there lacks tools to design or predict selective ligands. REST2-MD can identify selective μOR agonists and thus be used for ligand screening. Although it is more costly than docking or standard MD, it provides mechanistic and dynamics insights into the ligand actions, which is essential for the subsequent ligand optimization.

This study highlights the dynamic and allosteric details of μOR pre-activation upon agonist binding, prior to the coupling of intracellular signaling partners. The pre-activation stage is crucial for drug design because it is dictated by the ligands. Nevertheless, it is highly dynamic and inaccessible to X-ray crystallography or CryoEM. We took advantage of 2D HMQC NMR and enhanced-sampling MD to capture conformational dynamic patterns during the pre-activation, which differentiate the partial and the selective agonists from the full unselective ones. The phenomenon that selective or partial ligands stabilize distinct receptor conformations has been reported for the angiotensin II receptor 1 (during pre-activation) (Wingler et al., 2019), the glucagon-like peptide-1 receptor (in fully active state) (Liang et al., 2018) and the β2AR (partial and selective agonism in fully active state) (Masureel et al., 2018). One drawback of our approaches is the loss of temporal information. Nevertheless, it has been shown that selective agonism in μOR is not controlled by binding or signaling kinetics, suggesting a mechanism dictated by receptor conformations (Pedersen et al., 2020).

Most of the findings here are independent of Nb33, except for the interplay observed between the agonists and Nb33 (between the LBD and G protein binding site), the mechanism of which remains obscure. The process of G protein binding likely determines the G protein subtype selectivity through transient GPCR-G protein interactions or intermediate conformations (Du et al., 2019; Liu et al., 2019b), but this is beyond the scope of the current study. Without Nb33 or G proteins, however, our NMR and REST2-MD results coherently and robustly illustrated the specific conformational dynamics underlying the partial and selective agonisms. The mechanism relies on highly-conserve amino-acid motifs, which may be common for other class A GPCRs.

ACKNOWLEDGEMENTS

We acknowledge support from INSERM (France, S.G.), CNRS (France, H.D.), the National Institutes of Health (USA, grant NIDA-DA036246 to S.G.), the German Research Foundation (Deutsche Forschungsgemeinschaft, grant CO 1715/1-1 to X.C.) and the UCA-Jedi program (France, grant ANR-15-IDEX-01 to X.C. and J.G.). The CBS is a member of the French Infrastructure for Integrated Structural Biology (FRISBI), supported by the National Research Agency (ANR-10-INBS-05) and is a GIS-IBIsA platform. We also thank Prof. Peter Gmeiner for providing Bu72 and PZM21, and GENCI-CINES (France) for providing access to the supercomputer OCCIGEN (grant A0080711387 to J.G).

AUTHOR CONTRIBUTIONS

S.G. and R.S. designed the research. J.H., I.V-B., F.P., J. S-P. and R.S. designed expressed and purified the proteins. D.M. performed and analyzed cell-based assays. H.D. and R.S. performed and analyzed NMR data. X.C. performed the MD simulations. J.G. helped X.C. analyze the MD simulation data. X.C, S.G. and R.S. wrote the manuscript. All authors contributed to editing of the manuscript.

DECLARATION OF INTERESTS

The authors declare no competing interests.

REFERENCES

Casiraghi, M., Damian, M., Lescop, E., Point, E., Moncoq, K., Morellet, N., Levy, D., Marie, J., Guittet, E., Baneres, J.L., *et al.* (2016). Functional Modulation of a G Protein-Coupled Receptor Conformational Landscape in a Lipid Bilayer. J Am Chem Soc *138*, 11170-11175.

Clark, L.D., Dikiy, I., Chapman, K., Rodstrom, K.E., Aramini, J., LeVine, M.V., Khelashvili, G., Rasmussen, S.G., Gardner, K.H., and Rosenbaum, D.M. (2017). Ligand modulation of sidechain dynamics in a wild-type human GPCR. Elife *6*.

Cong, X., Cheron, J.B., Golebiowski, J., Antonczak, S., and Fiorucci, S. (2019). Allosteric Modulation Mechanism of the mGluR5 Transmembrane Domain. Journal of chemical information and modeling.

Cong, X., Fiorucci, S., and Golebiowski, J. (2018). Activation Dynamics of the Neurotensin G Protein-Coupled Receptor 1. Journal of chemical theory and computation *14*, 4467-4473.

Cong, X., and Golebiowski, J. (2018). Allosteric Na(+)-binding site modulates CXCR4 activation. Physical chemistry chemical physics : PCCP *20*, 24915-24920.

Conibear, A.E., and Kelly, E. (2019). A Biased View of mu-Opioid Receptors? Mol Pharmacol *96*, 542-549.

Cowan, A., Doxey, J.C., and Harry, E.J. (1977a). The animal pharmacology of buprenorphine, an oripavine analgesic agent. Br J Pharmacol *60*, 547-554.

Cowan, A., Lewis, J.W., and Macfarlane, I.R. (1977b). Agonist and antagonist properties of buprenorphine, a new antinociceptive agent. Br J Pharmacol *60*, 537-545.

Delaglio, F., Grzesiek, S., Vuister, G.W., Zhu, G., Pfeifer, J., and Bax, A. (1995). NMRPipe: a multidimensional spectral processing system based on UNIX pipes. J Biomol NMR *6*, 277-293.

DeWire, S.M., Yamashita, D.S., Rominger, D.H., Liu, G., Cowan, C.L., Graczyk, T.M., Chen, X.T., Pitis, P.M., Gotchev, D., Yuan, C.*, et al.* (2013). A G protein-biased ligand at the mu-opioid receptor is potently analgesic with reduced gastrointestinal and respiratory dysfunction compared with morphine. J Pharmacol Exp Ther *344*, 708-717.

Dickson, C.J., Madej, B.D., Skjevik, A.A., Betz, R.M., Teigen, K., Gould, I.R., and Walker, R.C. (2014). Lipid14: The Amber Lipid Force Field. J Chem Theory Comput *10*, 865-879.

Du, Y., Duc, N.M., Rasmussen, S.G.F., Hilger, D., Kubiak, X., Wang, L., Bohon, J., Kim, H.R., Wegrecki, M., Asuru, A.*, et al.* (2019). Assembly of a GPCR-G Protein Complex. Cell *177*, 1232-1242 e1211.

Eddy, M.T., Lee, M.Y., Gao, Z.G., White, K.L., Didenko, T., Horst, R., Audet, M., Stanczak, P., McClary, K.M., Han, G.W.*, et al.* (2018). Allosteric Coupling of Drug Binding and Intracellular Signaling in the A2A Adenosine Receptor. Cell *172*, 68-80 e12.

Emmerson, P.J., Liu, M.R., Woods, J.H., and Medzihradsky, F. (1994). Binding affinity and selectivity of opioids at mu, delta and kappa receptors in monkey brain membranes. J Pharmacol Exp Ther *271*, 1630-1637.

Frisch, M.J., Trucks, G.W., Schlegel, H.B., Scuseria, G.E., Robb, M.A., Cheeseman, J.R., Scalmani, G., Barone, V., Mennucci, B., Petersson, G.A.*, et al.* (2009). Gaussian 09, Revision A.02. (Wallingford CT).

Gillis, A., Gondin, A.B., Kliewer, A., Sanchez, J., Lim, H.D., Alamein, C., Manandhar, P., Santiago, M., Fritzwanker, S., Schmiedel, F.*, et al.* (2020). Low intrinsic efficacy for G protein activation can explain the improved side effect profiles of new opioid agonists. Sci Signal *13*.

Gordon, J.C., Myers, J.B., Folta, T., Shoja, V., Heath, L.S., and Onufriev, A. (2005). H++: a server for estimating pKas and adding missing hydrogens to macromolecules. Nucleic Acids Res *33*, W368-371.

Handa, B.K., Land, A.C., Lord, J.A., Morgan, B.A., Rance, M.J., and Smith, C.F. (1981). Analogues of beta-LPH61-64 possessing selective agonist activity at mu-opiate receptors. Eur J Pharmacol *70*, 531-540.

Huang, W., Manglik, A., Venkatakrishnan, A.J., Laeremans, T., Feinberg, E.N., Sanborn, A.L., Kato, H.E., Livingston, K.E., Thorsen, T.S., Kling, R.C.*, et al.* (2015). Structural insights into micro-opioid receptor activation. Nature *524*, 315-321.

Huang, W., Masureel, M., Qu, Q., Janetzko, J., Inoue, A., Kato, H.E., Robertson, M.J., Nguyen, K.C., Glenn, J.S., Skiniotis, G.*, et al.* (2020). Structure of the neurotensin receptor 1 in complex with beta-arrestin 1. Nature *579*, 303-308.

Isogai, S., Deupi, X., Opitz, C., Heydenreich, F.M., Tsai, C.J., Brueckner, F., Schertler, G.F., Veprintsev, D.B., and Grzesiek, S. (2016). Backbone NMR reveals allosteric signal transduction networks in the beta1-adrenergic receptor. Nature *530*, 237-241.

Jorgensen, W.L., Chandrasekhar, J., Madura, J.D., Impey, R.W., and Klein, M.L. (1983). Comparison of Simple Potential Functions for Simulating Liquid Water. J Chem Phys *79*, 926-935.

Joung, I.S., and Cheatham, T.E. (2008). Determination of alkali and halide monovalent ion parameters for use in explicitly solvated biomolecular simulations. J Phys Chem B *112*, 9020-9041.

Katritch, V., Fenalti, G., Abola, E.E., Roth, B.L., Cherezov, V., and Stevens, R.C. (2014). Allosteric sodium in class A GPCR signaling. Trends Biochem Sci *39*, 233-244.

Kliewer, A., Gillis, A., Hill, R., Schmiedel, F., Bailey, C., Kelly, E., Henderson, G., Christie, M.J., and Schulz, S. (2020). Morphine-induced respiratory depression is independent of beta-arrestin2 signalling. Br J Pharmacol *177*, 2923-2931.

Kliewer, A., Schmiedel, F., Sianati, S., Bailey, A., Bateman, J.T., Levitt, E.S., Williams, J.T., Christie, M.J., and Schulz, S. (2019). Phosphorylation-deficient G-protein-biased mu-opioid receptors improve analgesia and diminish tolerance but worsen opioid side effects. Nat Commun *10*, 367.

Koehl, A., Hu, H., Maeda, S., Zhang, Y., Qu, Q., Paggi, J.M., Latorraca, N.R., Hilger, D., Dawson, R., Matile, H.*, et al.* (2018). Structure of the micro-opioid receptor-Gi protein complex. Nature *558*, 547-552.

Kofuku, Y., Ueda, T., Okude, J., Shiraishi, Y., Kondo, K., Mizumura, T., Suzuki, S., and Shimada, I. (2014). Functional dynamics of deuterated beta2 -adrenergic receptor in lipid bilayers revealed by NMR spectroscopy. Angew Chem Int Ed Engl *53*, 13376-13379.

Latorraca, N.R., Venkatakrishnan, A.J., and Dror, R.O. (2017). GPCR Dynamics: Structures in Motion. Chem Rev *117*, 139-155.

Lee, Y., Warne, T., Nehme, R., Pandey, S., Dwivedi-Agnihotri, H., Chaturvedi, M., Edwards, P.C., Garcia-Nafria, J., Leslie, A.G.W., Shukla, A.K.*, et al.* (2020). Molecular basis of beta-arrestin coupling to formoterol-bound beta1-adrenoceptor. Nature *583*, 862-866.

Liang, Y.L., Khoshouei, M., Glukhova, A., Furness, S.G.B., Zhao, P., Clydesdale, L., Koole, C., Truong, T.T., Thal, D.M., Lei, S.*, et al.* (2018). Phase-plate cryo-EM structure of a biased agonist-bound human GLP-1 receptor-Gs complex. Nature *555*, 121-125.

Lindorff-Larsen, K., Piana, S., Palmo, K., Maragakis, P., Klepeis, J.L., Dror, R.O., and Shaw, D.E. (2010). Improved side-chain torsion potentials for the Amber ff99SB protein force field. Proteins *78*, 1950-1958.

Liu, X., Ahn, S., Kahsai, A.W., Meng, K.C., Latorraca, N.R., Pani, B., Venkatakrishnan, A.J., Masoudi, A., Weis, W.I., Dror, R.O.*, et al.* (2017). Mechanism of intracellular allosteric beta2AR antagonist revealed by X-ray crystal structure. Nature *548*, 480-484.

Liu, X., Masoudi, A., Kahsai, A.W., Huang, L.Y., Pani, B., Staus, D.P., Shim, P.J., Hirata, K., Simhal, R.K., Schwalb, A.M.*, et al.* (2019a). Mechanism of beta2AR regulation by an intracellular positive allosteric modulator. Science *364*, 1283-1287.

Liu, X., Xu, X., Hilger, D., Aschauer, P., Tiemann, J.K.S., Du, Y., Liu, H., Hirata, K., Sun, X., Guixa-Gonzalez, R.*, et al.* (2019b). Structural Insights into the Process of GPCR-G Protein Complex Formation. Cell *177*, 1243-1251 e1212.

Manglik, A., Kim, T.H., Masureel, M., Altenbach, C., Yang, Z., Hilger, D., Lerch, M.T., Kobilka, T.S., Thian, F.S., Hubbell, W.L.*, et al.* (2015). Structural Insights into the Dynamic Process of beta2-Adrenergic Receptor Signaling. Cell *161*, 1101-1111.

Manglik, A., Kruse, A.C., Kobilka, T.S., Thian, F.S., Mathiesen, J.M., Sunahara, R.K., Pardo, L., Weis, W.I., Kobilka, B.K., and Granier, S. (2012). Crystal structure of the μ-opioid receptor bound to a morphinan antagonist. Nature *485*, 321-326.

Manglik, A., Lin, H., Aryal, D.K., McCorvy, J.D., Dengler, D., Corder, G., Levit, A., Kling, R.C., Bernat, V., Hubner, H.*, et al.* (2016). Structure-based discovery of opioid analgesics with reduced side effects. Nature *537*, 185-190.

Masureel, M., Zou, Y., Picard, L.P., van der Westhuizen, E., Mahoney, J.P., Rodrigues, J., Mildorf, T.J., Dror, R.O., Shaw, D.E., Bouvier, M.*, et al.* (2018). Structural insights into binding specificity, efficacy and bias of a beta2AR partial agonist. Nat Chem Biol *14*, 1059-1066.

Neilan, C.L., Husbands, S.M., Breeden, S., Ko, M.C., Aceto, M.D., Lewis, J.W., Woods, J.H., and Traynor, J.R. (2004). Characterization of the complex morphinan derivative BU72 as a high efficacy, long-lasting mu-opioid receptor agonist. Eur J Pharmacol *499*, 107-116.

Nygaard, R., Zou, Y., Dror, R.O., Mildorf, T.J., Arlow, D.H., Manglik, A., Pan, A.C., Liu, C.W., Fung, J.J., Bokoch, M.P.*, et al.* (2013). The dynamic process of beta(2)-adrenergic receptor activation. Cell *152*, 532-542.

Okude, J., Ueda, T., Kofuku, Y., Sato, M., Nobuyama, N., Kondo, K., Shiraishi, Y., Mizumura, T., Onishi, K., Natsume, M.*, et al.* (2015). Identification of a Conformational Equilibrium That Determines the Efficacy and Functional Selectivity of the mu-Opioid Receptor. Angewandte Chemie *54*, 15771-15776.

Patriksson, A., and van der Spoel, D. (2008). A temperature predictor for parallel tempering simulations. Phys. Chem. Chem. Phys. *10*, 2073-2077.

Pedersen, M.F., Wrobel, T.M., Marcher-Rorsted, E., Pedersen, D.S., Moller, T.C., Gabriele, F., Pedersen, H., Matosiuk, D., Foster, S.R., Bouvier, M.*, et al.* (2020). Biased agonism of clinically approved mu-opioid receptor agonists and TRV130 is not controlled by binding and signaling kinetics. Neuropharmacology *166*, 107718.

Raehal, K.M., Schmid, C.L., Groer, C.E., and Bohn, L.M. (2011). Functional selectivity at the mu-opioid receptor: implications for understanding opioid analgesia and tolerance. Pharmacological reviews *63*, 1001-1019.

Schmid, C.L., Kennedy, N.M., Ross, N.C., Lovell, K.M., Yue, Z., Morgenweck, J., Cameron, M.D., Bannister, T.D., and Bohn, L.M. (2017). Bias Factor and Therapeutic Window Correlate to Predict Safer Opioid Analgesics. Cell *171*, 1165-1175 e1113.

Schott-Verdugo, S., and Gohlke, H. (2019). PACKMOL-Memgen: A Simple-To-Use, Generalized Workflow for Membrane-Protein-Lipid-Bilayer System Building. J Chem Inf Model *59*, 2522-2528.

Sena, D.M., Jr., Cong, X., Giorgetti, A., Kless, A., and Carloni, P. (2017). Structural heterogeneity of the mu-opioid receptor's conformational ensemble in the apo state. Scientific reports *8*, 45761.

Shimada, I., Ueda, T., Kofuku, Y., Eddy, M.T., and Wuthrich, K. (2019). GPCR drug discovery: integrating solution NMR data with crystal and cryo-EM structures. Nat Rev Drug Discov *18*, 59-82.

Sounier, R., Mas, C., Steyaert, J., Laeremans, T., Manglik, A., Huang, W., Kobilka, B.K., Demene, H., and Granier, S. (2015). Propagation of conformational changes during mu-opioid receptor activation. Nature *524*, 375-378.

Staus, D.P., Hu, H., Robertson, M.J., Kleinhenz, A.L.W., Wingler, L.M., Capel, W.D., Latorraca, N.R., Lefkowitz, R.J., and Skiniotis, G. (2020). Structure of the M2 muscarinic receptor-beta-arrestin complex in a lipid nanodisc. Nature *579*, 297-302.

Traynor, J.R., and Nahorski, S.R. (1995). Modulation by mu-opioid agonists of guanosine-5'-O-(3-[35S]thio)triphosphate binding to membranes from human neuroblastoma SH-SY5Y cells. Mol Pharmacol *47*, 848-854.

Tribello, G.A., Bonomi, M., Branduardi, D., Camilloni, C., and Bussi, G. (2014). PLUMED 2: New feathers for an old bird. Computer Physics Communications *185*, 604-613.

Trott, O., and Olson, A.J. (2010). AutoDock Vina: improving the speed and accuracy of docking with a new scoring function, efficient optimization, and multithreading. J Comput Chem *31*, 455-461.

Van Der Spoel, D., Lindahl, E., Hess, B., Groenhof, G., Mark, A.E., and Berendsen, H.J. (2005). GROMACS: fast, flexible, and free. J. Comput. Chem. *26*, 1701-1718.

Vanni, S., Neri, M., Tavernelli, I., and Rothlisberger, U. (2010). A conserved protonation-induced switch can trigger "ionic-lock" formation in adrenergic receptors. J Mol Biol *397*, 1339-1349.

Vranken, W.F., Boucher, W., Stevens, T.J., Fogh, R.H., Pajon, A., Llinas, M., Ulrich, E.L., Markley, J.L., Ionides, J., and Laue, E.D. (2005). The CCPN data model for NMR spectroscopy: development of a software pipeline. Proteins *59*, 687-696.

Wang, J.M., Cieplak, P., and Kollman, P.A. (2000). How well does a restrained electrostatic potential (RESP) model perform in calculating conformational energies of organic and biological molecules? J Comput Chem *21*, 1049-1074.

Wang, J.M., Wolf, R.M., Caldwell, J.W., Kollman, P.A., and Case, D.A. (2004). Development and testing of a general amber force field. J Comput Chem *25*, 1157-1174.

Wang, L., Friesner, R.A., and Berne, B.J. (2011). Replica exchange with solute scaling: a more efficient version of replica exchange with solute tempering (REST2). J Phys Chem B *115*, 9431-9438.

Weis, W.I., and Kobilka, B.K. (2018). The Molecular Basis of G Protein-Coupled Receptor Activation. Annu Rev Biochem *87*, 897-919.

Wingler, L.M., Elgeti, M., Hilger, D., Latorraca, N.R., Lerch, M.T., Staus, D.P., Dror, R.O., Kobilka, B.K., Hubbell, W.L., and Lefkowitz, R.J. (2019). Angiotensin Analogs with Divergent Bias Stabilize Distinct Receptor Conformations. Cell *176*, 468-478 e411.

Xu, J., Hu, Y., Kaindl, J., Risel, P., Hubner, H., Maeda, S., Niu, X., Li, H., Gmeiner, P., Jin, C*., et al.* (2019). Conformational Complexity and Dynamics in a Muscarinic Receptor Revealed by NMR Spectroscopy. Molecular cell.

Ye, L., Van Eps, N., Zimmer, M., Ernst, O.P., and Prosser, R.S. (2016). Activation of the A2A adenosine G-protein-coupled receptor by conformational selection. Nature *533*, 265-268.

Yin, W., Li, Z., Jin, M., Yin, Y.L., de Waal, P.W., Pal, K., Yin, Y., Gao, X., He, Y., Gao, J., *et al.* (2019). A complex structure of arrestin-2 bound to a G protein-coupled receptor. Cell Res *29*, 971-983.

Yuan, S., Palczewski, K., Peng, Q., Kolinski, M., Vogel, H., and Filipek, S. (2015). The mechanism of ligand-induced activation or inhibition of mu- and kappa-opioid receptors. Angew Chem Int Ed Engl *54*, 7560-7563.

Yudin, Y., and Rohacs, T. (2019). The G-protein-biased agents PZM21 and TRV130 are partial agonists of mu-opioid receptor-mediated signalling to ion channels. Br J Pharmacol *176*, 3110-3125.

STAR METHODS

KEY RESOURCES TABLE

REAGENT or RESOURCE	SOURCE	IDENTIFIER
Bacterial and virus strains		
E. coli cells BL21(DE3)	NEB	C2527
E. coli cells DH5α	NEB	C2987
E. coli cells DH10Bac	invitrogen	10361012
Chemicals, peptides, and recombinant proteins		
pFastBac vector	Thermofisher	Cat#10712024
pCDNA3.1 vector	Thermofisher	Cat#V79020
pVL1392 vector	Expression Systems	91-030
Tag-Lite buffer 5x	PerkinElmer/Cisbio	Cat#LABMED
SNAP-Lumi4-Tb	PerkinElmer/Cisbio	Cat#SSNPTBX
SNAP-red	PerkinElmer/Cisbio	Cat#SSNPREDF
Coelenterazine H	invitrogen	Cat#C6780
Naltrexone-d2	PerkinElmer/Cisbio	Cat#L0005RED
Iodoacetamide	Sigma	Cat#I6125
Leupetin	Euromedex	Cat#SP-04-2217
Benzamidine	Sigma	Cat#B6506
Phenylmethanesulfonyl fluoride (PMSF)	Sigma	Cat#P7626
n-dodecyl-beta-D-maltopyranoside (DDM)	Anatrace	Cat#D310
Lauryl Maltose Neopentyl (MNG)	Anatrace	Cat#NG310
Cholesterol hemisucinate (CHS)	Sigma	Cat#C6512
Sodium Cholate hydrate	Sigma	Cat#C1254
ANTI-FLAG® M1 Agarose Affinity Gel	Sigma-Aldrich	Cat#A4596
FLAG peptide	Covalab	https://www.covalab.com/peptide-synthesis
ESF921 culture medium, Methionine Deficient	Expression Systems	Cat#96-200
EX-CELL420 Serum-Free Medium	Sigma-Aldrich	Cat#14420
L-Methionine (methyl-^{13}C, 99%)	Eurisotop	Cat#DLM-206-0
Deuterium oxide (D_2O)	Eurisotop	Cat#D214
2,2-dimethyl-2-silapentane-5-sulfonic acid (DSS)	Eurisotop	Cat#DLM-32
HEPES (D18, 98%)	Eurisotop	Cat#DLM-3786
Dimethyl sulfoxide-d_6	Sigma-Aldrich	Cat#151874
Formaldehyde (^{13}C, 99%) 20 wt.%	Sigma-Aldrich	Cat#489417
Sodium cyanoborohdride ($NaBH_3CN$)	Sigma-Aldrich	Cat#156159
Buprenorphine hydrochloride	Sigma-Aldrich	Cat#B9275
TRV130 hydrochloride	Cliniscience	Cat#HY-16655A
[D-Ala^2, N-Me-Phe^4, Gly^5-ol]-Enkephalin acetate salt (DAMGO)	Sigma-Aldrich	Cat#E7384
BU72	Prof. Peter Gmeiner	N/A
PZM21	Prof. Peter Gmeiner	N/A
Experimental models: cell lines		
insect cell line Sf9	Life Technologies	Cat#11496015
HEK293 human cells	ATCC	CRL-1573
Recombinant DNA		
pVL1392-μOR-2x-M72T	Sounier et al., 2015	N/A
pFastBac-μOR-2x-M72T	Sounier et al., 2015	N/A
pFastBac-μOR-2x-M72T-mutant	This study	N/A
pcDNA-μOR-YFP	This study	N/A
pcDNA-SNAP-μOR	This study	N/A
pcDNA-μOR-2x-M72T	This study	N/A

pcDNA-GRK2-RLuc	Arpège	https://www.arpege.cnrs.fr/
pcDNA-FLAG-Gβ2	Arpège	https://www.arpege.cnrs.fr/
pcDNA-Gγ1-Venus	Arpège	https://www.arpege.cnrs.fr/
pcDNA-Venus-Gγ2	Arpège	https://www.arpege.cnrs.fr/
pcDNA-Gαi1-RLuc8	Arpège	https://www.arpege.cnrs.fr/
pcDNA-Gαi2-RLuc8	Arpège	https://www.arpege.cnrs.fr/
pcDNA-Gαi3-RLuc8	Arpège	https://www.arpege.cnrs.fr/
pcDNA-GαOA-RLuc8	Arpège	https://www.arpege.cnrs.fr/
pcDNA-GαOB-RLuc8	Arpège	https://www.arpege.cnrs.fr/
pcDNA-arrestin1-RLuc	Arpège	https://www.arpege.cnrs.fr/
pcDNA-arrestin2-RLuc	Arpège	https://www.arpege.cnrs.fr/
pMal-p2x-Nb33	Sounier et al., 2015	N/A
Software and algorithms		
PyMOL	Schrödinger	https://pymol.org/2/
Prism v.6.0	GraphPad Software	https://www.graphpad.com/scientific-software/prism/
NMRpipe	Delaglio et al., 1995	https://www.ibbr.umd.edu/nmrpipe/install.html
CCPNMR Analysis v3.0	Vranken et al., 2005	https://www.ccpn.ac.uk/v2-software/software/analysis
Autodock Vina	Trott and Olson, 2010	http://vina.scripps.edu/
H++ server	Gordon et al., 2005	http://biophysics.cs.vt.edu/
GROMACS 5.1	Van Der Spoel et al., 2005	https://www.gromacs.org
PLUMED 2.3	Tribello et al., 2014	https://www.plumed.org/
PACKMOL-Memgen	Schott-Verdugo and Gohlke, 2019	https://github.com/alanwilter/acpype/blob/master/amber19-0_linux/bin/packmol-memgen

RESOURCE AVAILABILITY

Lead contact

Further information and requests for reagents should be directed to and will be fulfilled by the lead contact, Rémy Sounier (remy.sounier@igf.cnrs.fr)

Materials availability

DNA constructs generated by the authors can be obtained upon request from the Lead Contact, but we may require a payment and/or a completed Materials Transfer Agreement if there is potential for commercial application.

Data and code availability

The article includes all datasets generated or analyzed during this study.

EXPERIMENTAL MODEL AND SUBJECT DETAILS

Mouse μOR, human Gαi1 and Gβγ were expressed in Sf9 cells infected with recombinant baculovirus (pFastBac, Invitrogen and BestBac, Expression Systems).

QUANTIFICATION AND STATISTICAL ANALYSIS

Quantification and statistical analyses of data are described in Method Details and Figure legends.

METHOD DETAILS

Cell lines and transfection

HEK293 cells were grown in Dulbecco's Modified Eagle's Medium (DMEM, Life Technologies) supplemented with 10% fetal bovine serum (FBS, Life Technologies) without antibiotics at 37°C, 5% CO_2. Transient transfection was performed using lipofectamine2000 (Invitrogen Life Technologies). Depending on the assay, HEK293 cells were stimulated 24h or 48h after transfection. For G protein activation and GRK2 recruitment, cells were seeded into a 6-well plate for 24h at a density of 750,000 cells per well. Cells were then detached, seeded and incubated for 24h in a 96-well white plate coated with poly-$_L$-Ornithine at a density of 40,000 cells per well. For binding, β-arrestins recruitment and internalization assays, cells were directly transfected into a 96-well white plate coated with poly-$_L$-Ornithine at a density of 40,000 cells per well following manufacturer's recommended protocol. For binding assay on membrane and solubilized receptors cells were transfected using electroporation. Electroporation was performed in a volume of 400 μL with a total 5 μg SNAP-μOR plasmid and 20,000,000 cells in electroporation buffer (50 mM K_2HPO_4, 20 mM CH_3COOK, and 20 mM KOH, pH 7.4). After electroporation (260 V, 1 mF, Bio–Rad Gene Pulser electroporator), cells were resuspended in 15 mL DMEM supplemented with 10% FBS in T150 culture dishes (pretreated with Poly-L-Ornithine) for 24 h.

G protein activation assay

The cells were transfected with 4 plasmids encoding the mouse μOR receptor (Flag-μOR-2x), the β2 and Venus-γ2 G protein subunits and the Gα protein fused with a donor at a 1:1:1:1 ratio. Gαi1, Gαi2, Gαi3, GαOA and GαOB was fused to *Renilla Luciferase2* (Rluc8 provided by the ARPEGE platform). 24 h after transfection, cells were washed twice with PBS. Basal conditions were achieved by the addition of PBS solutions, followed by Coelenterazine H at a final concentration of 5 μM. To evaluate

the effects of the μOR agonists, the addition of Coelenterazine H was followed by stimulation with different agonists. Activation of the μOR promotes dissociation of the Gαβγ protein complex resulting in the Bioluminescence resonance energy transfer (BRET) signal decay. BRET between Rluc8 and Venus was measured after the addition of the Rluc8 substrate Coelenterazine H. BRET readings were collected using a Mithras LB940 plate reader (Berthold technologies) and the reading chamber was maintained at 37 °C throughout the entire reading time. The BRET signal was calculated by the ratio of emission of Venus (535 nm) to Rluc8 (480 nm):

$$mBRET = ((Ratio\ 535/480)_{assay} - (Ratio\ 535/480)_{Rluc8\ alone}) \times 1000.$$

GRK2 recruitment assay

The cells were transfected with 2 plasmids encoding the human μOR receptor fused to YFP at the C-terminal, and GRK2 was fused to *Renilla Luciferase2* (provided by the ARPEGE platform). 24 h after transfection, cells were washed twice with PBS. The cells were incubated with Coelenterazine H at a final concentration of 5 μM, followed by stimulation with agonists before the BRET readings were captured. Recruitment of GRK2 is assessed by an increase in the BRET signal.

β-arrestins recruitment assay

The cells were transfected with 2 plasmids encoding the human μOR receptor fused to YFP at the C-terminal, and β-arrestin-1/β-arrestin-2 was fused to *Renilla Luciferase1* at the N-terminal (provided by Dr. M. Scott to the ARPEGE platform). 24 h after transfection, cells were washed twice with PBS. The cells were incubated with Coelenterazine H at a final concentration of 5 μM, followed by stimulation with agonists before the BRET readings were captured. Recruitments of β-arrestin-1 and β-arrestin-2 are assessed by an increase in the BRET signal.

Internalization assay

The cells were transfected with one plasmid encoding the SNAP-μOR receptor. 24 hours after transfection, SNAP-μOR cells were washed with Tag-Lite buffer (CisBio Bioassays) and incubated at 37°C with benzylguanine-Lumi4-Tb (SNAP-Lumi4-Tb) at a concentration of 100 nM during 1 hour. The cells were washed 4 times with Tag-Lite buffer and then incubated with μOR agonists diluted in fluorescein buffer (24 μM). Reading was performed at 37°C on an Infinite F500® plate reader (TECAN) with an excitation at 337 nm and emission at 620 nm. Receptor internalization was monitored by time-resolved fluorescent resonance energy transfer (TR-FRET) at 37 °C during 70–80 min. The signal was calculated by the ratio of emission of terbium cryptate (620 nm) to fluorescein (520 nm): $\Delta R = (Ratio\ 620/520) \times 10{,}000$.

Fluorescent ligand-binding assay on living cells

HEK293 cells transfected with SNAP-μOR plasmid were seeded at a density of 40,000 cells per well in 96-well white plates coated with poly-$_L$-Ornithine. 24h after transfection, SNAP-μOR was labeled 1 h at 37°C with 100nM SNAP-Lumi4-Tb diluted in Tag-lite labeling buffer. Fluorescent naltrexone and agonists were diluted in Tag-lite labeling buffer. A fixed concentration of fluorescent naltrexone-d2 was determined (0.5 nM = K_d) and used. Increasing concentration of agonists was added prior to the addition of fluorescent naltrexone-d2 in the plates containing labeled cells. Plates were incubated overnight at 4°C before homogenous time-resolved Fluorescent (HTRF) signal detection. HTRF detection was performed on a PHERAstar (BMG labtechnologies). The signal was collected both at 665 nm and 620 nm. HTRF ratio was obtained by dividing the acceptor signal at 665 nm by the donor signal at 620 nm and multiplying this value by 10,000. Data obtained were then analyzed using GraphPad Prism (GraphPad Software, Inc., San Diego, CA).

Membrane preparation and SNAP labeling

Twenty-four hours after transfection cells were washed once with PBS solution, scraped and then collected by centrifugation 5 minutes at 300 g. The cell pellet was resuspended in 20 mL lysis buffer (10 mM HEPES, 1 mM EDTA) and homogenized using an electric homogenizer on ice. After centrifugation 5 min at 1,000g at 4 °C, the pellet was discarded and the supernatant was centrifuged at 30,000 g for 30 min at 4 °C. The resulting pellet was resuspended in 2 mL of Tag-Lite buffer containing 300 nM BG-Lumi4-Tb and incubated for 1 hour at 4 °C under circle rotator. Membranes were then resuspensed in 2 mL PBS to remove the excess of BG-Lumi4-Tb and centrifuged at 30,000 g for 30 min on a bentchtop centrifuge. This step was reproduced twice. Protein concentration was determined by BCA using BSA as standard. SNAP-μOR membranes were aliquoted and stored at -80 °C.

Fluorescent ligand-binding assay on solubilized receptors

SNAP-μOR membranes were resuspended in solubilization buffer (see below for composition details) and stirred 1 hour at 4 °C. After centrifugation at 36,000 g for 20 min at 4 °C, the solute material was complemented with 2 mM $CaCl_2$ and loaded on M1 antibody Resin. Detergent exchange protocol was performed (see below for details) and solubilized SNAP-μOR was eluted from M1 antibody resin. Naltrexone-d2 binding affinity towards solubilized SNAP-μOR was determined at 3 nM against 0.5 nM on living cells and 1 nM HEK293 cell membranes. Freshly prepared solubilized SNAP-μOR were incubated with increasing concentrations of agonists and a fixed concentration of fluorescent naltrexone-d2 (12 nM = K_d) before HTRF signal detection.

(Met-ε)-[$^{13}CH_3$]-μOR-2x M72T expression

We generated a μ-OR mouse construct with features designed to enhance stability for NMR spectroscopy. A tobacco etch virus (TEV) protease recognition site was introduced after residue 51, and a human rhinovirus 3C protease site after residue 358. Receptor expression was largely improved by using a M72$^{1.36}$T single-point mutation as previously reported (Sounier et al., 2015). A FLAG tag was added to the amino terminus and an 8 × His tag was appended to the carboxy terminus (μOR-2x). Recombinant baculoviruses were generated using the BestBac baculovirus system according to manufacturer's instructions (Expression Systems). For the assignment of all other mutants, we used the pFastBac baculovirus system (ThermoFischer). High titer baculoviruses encoding μOR-2x genes were used to infect *Sf*9 cells at a cell density of 4×10^6 cells per ml in suspension in methionine deficient media (Expression System) in the presence of 3 mM naloxone with ^{13}C methyl labelled methionine (Cambridge Isotope) added into the media at 250 $mg \cdot L^{-1}$ concentration. Cells were harvested by centrifugation 48 h post-infection and stored at -80 °C until purification.

(Met-ε)-[$^{13}CH_3$]-μOR-2x M72T purification

Cell pellets were resuspended in 10 mM Tris-HCl pH 7.5, 1 mM EDTA buffer containing 2 $mg \cdot mL^{-1}$ iodoacetamide and protease inhibitors without salt to lyse the cells by hypotonic lysis. Lysed cells were centrifuged (38,420 g) and the membranes were solubilized durinf 1h @ 4 °C using buffer containing 20 mM HEPES (pH 7.5), 200 mM NaCl, 0.5% (w/v) n-dodecyl-β-D-maltoside (DDM, Anatrace), 0.3% (w/v) CHAPS, 0.03% (w/v) choslesteryl-hemi-succinate (CHS, Sigma), 2 $mg \cdot mL^{-1}$ iodoacetamide and protease inhibitors. The solubilized receptor was loaded onto anti-Flag M1 column (Sigma) and washed thoroughly with DDM buffer containing 20 mM HEPES (pH 7.5), 100 mM NaCl, 0.1% (w/v) DDM, 0.03% (w/v) CHAPS, 0.015% (w/v) CHS and 2 mM $CaCl_2$. While on the M1 antibody resin, the receptor was exchanged into lauryl-maltose-neopentyl-glycol (MNG-14, Anatrace)

detergent-containing buffer composed of 20 mM HEPES (pH 7.5), 100 mM NaCl, 0.5% (w/v) MNG-14 and 0.01 % CHS. The detergent exchange was performed by washing the column with a series of seven buffers (3 CV each) made up of the following ratios (v/v) of MNG-14 buffer and DDM buffer: 0:1, 1:1, 4:1, 9:1, 19:1, 99:1 and MNG-14 exchange buffer alone. The column was then washed with 20x critical micelle concentration (cmc) MNG-14 buffer containing 20 mM HEPES (pH 7.4), 100 mM NaCl, 0.02% (w/v) MNG and 0.0004 % CHS and the bound receptor was eluted in the same buffer supplemented with 0.2 $mg \cdot mL^{-1}$ Flag peptide. To remove flexible amino and carboxy termini, TEV and 3C protease were added at a 1:5 and 1:10 protease:μOR-2x ratio by weight. The sample was incubated at 4 °C overnight in the presence of 100 μM of TCEP. We then used a negative Ni-NTA chromatography step to remove TEV and 3C proteases.

(Met-ε)-[$^{13}CH_3$]-μOR-2x M72T reductive methylation

Receptor preparation from the Ni-NTA flow through were incubated at 4 °C overnight with 10 mM ^{13}C-formaldehyde and 10 mM $NaBH_3CN$. Excess of reagent was eliminated by dialysis and (Met-ε)-[$^{13}CH_3$],(Lys-Nε,Nε)[$^{13}CH_3$,$^{13}CH_3$]-μOR ((^{13}C-M$^{\varepsilon}$,K^{me2})-μOR) was further purified by SEC chromatography in a buffer containing 0.01% MNG, 0.001% CHS, 20 mM HEPES pH 7.4 and 40 mM NaCl. The monodisperse peak was then concentrated to 30 to 60 μM final, and dialysed in 98.85% D_2O buffer with 0.01% MNG, 0.0004% CHS, 20 mM HEPES-d18 pH 7.4 (uncorrected) and 40 mM NaCl.

Nanobody Nb33 expression and purification

The DNA sequence of Nb33 was subcloned into a pMalp2x vector containing an N-terminal, 3C protease-cleavable maltose binding protein (MBP) tag and a C-terminal 8 × His tag. Plasmids were transformed into BL21(DE3) cells and protein expression induced in liquid broth (LB) by addition of IPTG to 0.5 mM at an OD_{600} of 0.6. Cells were harvested after overnight growth at 20°C by centrifugation at 6,000 g for 30 min. Cells were resuspended in 20 mM HEPES buffer (pH 7.5), 500 mM NaCl, 0.1 $mg \cdot mL^{-1}$ lysozyme and PMSF was added as a protease inhibitor before lysis by sonication. The cell lysate was centrifuged at 38,420 g for 30 min at 4 °C. The soluble fraction was isolated and was supplemented with imidazole to a final concentration of 20 mM. MBP–nanobody fusions were purified by Ni-NTA chromatography and MBP was removed using 3C protease. Cleaved MBP was separated from the nanobody by additional amylose purification and size exclusion chromatography in a buffer containing 20 mM HEPES pH 7.4 and 0.1 M NaCl.

NMR Spectroscopy

Final samples (~270 μl at 30–60 μM) were loaded into Shigemi microtubes susceptibility matched to D_2O. All data for ligands and mutant studies were acquired on 700 MHz Bruker Avance III spectrometers (Bruker, Rheinstetten, Germany), equipped with 5 mm cryogenic H/C/N/D probes with *z* axis gradient. ^{1}H-^{13}C correlation spectra were recorded using heteronuclear multiple-quantum coherence (HMQC) experiments in echo anti-echo mode. ^{13}C and ^{1}H chemical shifts and peak line widths in the HMQC spectra reveal the chemical and magnetic environments of the ^{13}C-methyl probes as well as their dynamic properties. Spectral widths in ω1 and ω2 were 8,417.5 Hz and 3,518.6 Hz at 700 MHz centred at 40 p.p.m. or 20 p.p.m. in the ^{13}C dimension. ^{13}C decoupling was performed with a GARP4 sequence. Typically, 134 complex points with 32–48 scans per FID were recorded, to ensure a 27-Hz resolution per point at 700 MHz before zero filling. The relaxation delay was set to 1.5 s. Thirty-two steady-state scans preceded data acquisition. Total collection time varied between 3 and 4 h, depending on the sample concentration. Spectra were processed using NMRPipe/NMRDraw software (Delaglio et al., 1995) and visualized using CCPNMR (Vranken et al., 2005). All ligands were dissolved in perdeuterated dimethyl d_6-sulfoxide (d_6-DMSO, Cambridge Isotope) to 100 mM and directly added to the sample in the Shigemi tube at a final concentration five-fold of receptor. Nb33

were concentrated to 0.6 mM and dialysed in 100% D_2O buffer with 0.01% MNG, 0.001% CHS, 20 mM HEPES-d18 pH 7.4 (uncorrected) and 40 mM NaCl. The nanobodies were added directly in the Shigemi tubes at a final concentration of two-fold of the receptor before data acquisition.

Molecular dynamics simulations

The initial coordinates of μOR were from the crystal structure of an inactive form (PDB: 4DKL). The ligands were docked to the initial μOR structure using Autodock Vina (Trott and Olson, 2010). Residues in the putative ligand-binding pocket were set flexible during docking. The protonation state of titrable residues were predicted at pH 6.5 using the H++ server (Gordon et al., 2005). The receptor-odorant complexes were embedded in a bilayer of POPC using PACKMOL-Memgen (Schott-Verdugo and Gohlke, 2019). Each system was solvated in a periodic 75 × 75 × 105 $Å^3$ box of explicit water and neutralized with 0.15 M of Na^+ and Cl^- ions. Effective point charges of the ligands were obtained by RESP fitting (Wang et al., 2000) of the electrostatic potentials calculated with the HF/6-31G* basis set using Gaussian 09 (Frisch et al., 2009). The Amber 99SB-ildn (Lindorff-Larsen et al., 2010), lipid 14 (Dickson et al., 2014) and GAFF (Wang et al., 2004) force fields were used for the proteins, the lipids and the ligands, respectively. The TIP3P (Jorgensen et al., 1983) and the Joung-Cheatham (Joung and Cheatham, 2008) models were used for the water and the ions, respectively.
After energy minimization, all-atom MD simulations were carried out using Gromacs 5.1 (Van Der Spoel et al., 2005) patched with the PLUMED 2.3 plugin (Tribello et al., 2014). Each system was gradually heated to 310 K and pre-equilibrated during 10 ns of brute-force MD in the *NPT*-ensemble. The replica exchange with solute scaling (REST2) (Wang et al., 2011) technique was employed to enhance the sampling with 48 replicas in the *NVT* ensemble. The protein and the ligands were considered as “solute” in the REST2 scheme–force constants of their van der Waals, electrostatic and dihedral terms were subject to scaling. The effective temperatures used for generating the REST2 scaling factors ranged from 310 K to 700 K, following a distribution calculated with the Patriksson-van der Spoel approach (Patriksson and van der Spoel, 2008). Exchange between replicas was attempted every 1000 simulation steps. This setup resulted in an average exchange probability of ~40%. We performed 50 ns × 48 replicas MD in the *NVT* ensemble for each system. The first 20 ns were discarded for equilibration. The original unscaled replica (at 310 K effective temperature) was collected and analyzed. Cluster analysis of the ligand binding pose was carried out on the non-restrained trajectory using the Gromacs Cluster tool. The middle structure of the most populated cluster was selected as the final binding pose.